Imaging Single Nanobubbles of H_2 and O_2 during the Overall Water Electrolysis with Single-Molecule Fluorescence Microscopy

Rui Hao‡, Yunshan Fan‡, Todd J. Anderson, and Bo Zhang*
Department of Chemistry, University of Washington, Seattle Washington 98115 United States

Corresponding author, zhangb@uw.edu
Phone: (1) 206 543 1767
Fax: (1) 206 685 8665
‡ These authors contributed equally to this work

Abstract. In this work, we describe the preparation and use of a thin metal film modified Indium Tin Oxide (ITO) electrode as a highly conductive, transparent, and electrocatalytically active electrode material for studying nanobubbles generated at the electrode/solution interface. Hydrogen and oxygen nanobubbles were generated from water electrolysis on the surface of a Au/Pd alloy modified ITO electrode. The formation of single H_2 and O_2 nanobubbles was imaged in real time during a potential scan using single-molecule fluorescence microscopy. Our results show that while O_2 nanobubbles can be detected at an early stage in the oxygen evolution reaction (OER), the formation of H_2 nanobubbles requires a significant overpotential. Our study shows that thin film coated ITO electrodes are simple to make and can be useful electrode substrates for (single molecule) spectroelectrochemistry research.

Introduction

As a carbon emission-free fuel, hydrogen gas from water electrolysis is attracting much attention in clean energy research.[1] Water electrolysis, which is comprised of the hydrogen evolution reaction (HER) and the oxygen evolution reaction (OER), remains an attractive and challenging topic in electrochemistry[2] with new electrocatalysts constantly being developed for both reactions.[3,4] Identifying the formation and growth of gas bubbles in HER and OER may influence their reaction dynamics,[5] several attempts have been made to design new interfaces for expedited gas removal.[6,7]

As gas nanobubbles are small and transparent at the nucleation stage, they are challenging to characterize in electrochemical systems.[8] Several approaches have been taken to characterize nanobubbles under ambient conditions. These include atomic force microscopy (AFM),[9] interference-enhanced optical microscopy,[10] fluorescence[11,12] and dark-field[13] microscopies, and surface-plasmon resonance (SPR) imaging.[14] Electrochemical methods have also been used to study single nanobubbles on an electrode.[15] Several groups have used nanopores to sense individual nanobubbles.[16,17,18] Optical methods, such as super-resolution fluorescence microscopy, have the unique ability to image the electrochemical interface with high spatial and temporal resolution.[19,20] Our group has used a single-molecule fluorescence labeling approach to image H_2 nanobubbles using total-internal reflection fluorescence (TIRF) microscopy.[21] Our results indicated that nucleation of H_2 nanobubbles could start at an early stage of the water reduction reaction. As many other TIRF-based electrochemical studies,[22] we used a transparent ITO electrode to generate H_2 molecules. Despite our success with H_2, however, we were unable to reproducibly image O_2 nanobubbles on ITO. This is likely due to ITO's low catalytic activity as it has been shown that ITO is known for its inertness in electrocatalytic reactions.[23,24]

Metals and metal alloys have been used as electrode materials for more than one hundred years. From voltaic cell to fuel cell, chlorine production to carbon dioxide reduction, metal-based electrodes are pivotal to numerous electrochemical reactions. It would be beneficial to develop suitable analytical methods to study nanoscale electrochemical processes at the metal/electrolyte interface.[25,26]

Identifying the limitation of using ITO in studying OER and other gas-evolving reactions with our single molecule nanobubble labeling method, in this study, we added a thin metal layer on ITO to enhance its catalytic activity without significantly sacrificing its transparence, a key property needed for highly sensitive single-molecule TIRF imaging. We aim to test our ability to use single-molecule fluorescence to image nanobubble generation at metal/electrolyte interface. A new type of transparent electrode consisting of a thin layer of gold/palladium on an ITO surface (*hereafter referred as Au/Pd-ITO*) was prepared and used to study the overall water electrolysis. Using single-molecule fluorescence imaging, both oxygen and hydrogen nanobubbles were observed from the HER and OER, respectively. We confirmed that oxygen nanobubbles could be generated at an early stage of the OER. The difference between nucleating the H_2 and O_2 nanobubbles was also discussed.

Experimental Section

Au/Pd-ITO Electrodes. Pieces of ITO-coated cover glass were rinsed three times each with DI water and ethanol. They were then coated for 90 seconds in a SPI-Module sputter coater equipped with an Au/Pd target (60:40, wt%). To achieve reproducible film thicknesses, the substrates were placed 40 mm from the target and a plasma current of 9 mA was maintained.

TIRF Microscopy. Single-molecule TIRF imaging was performed on an Olympus IX70 inverted microscope configured for TIRF using an Apo N 60× 1.49 NA objective and a 10 mW (2.5 kW/cm^2) 532 nm laser (CrystaLaser). An additional 1.5× magnification on the microscope was used during

imaging. The fluorescence images were optically filtered with an ET590/50m emission filter (Chroma Technology) and acquired on an Andor iXon3 EMCCD camera cooled to -85 °C. Images were recorded with an exposure time of 50 ms or a frame rate of 19.81 Hz. An electron multiplying amplifier gain of 300 and a preamplifier gain of 5.1 were used. The voltage waveform was generated by a Pine AFCBP1 potentiostat and applied across the working electrode (ITO or Au/Pd-ITO) and a Pt quasi-reference electrode (QRE). A thin polydimethylsiloxane (PDMS) film with a 2-mm-diameter hole was attached to the ITO surface to define the electrode area. A PCI-6251 (National Instruments) data acquisition card and a BNC-2090 breakout box were used to interface the potentiostat with the PC.

Image Analysis. Fluorescence images were analyzed using ThunderSTORM plug-in in ImageJ.[27] Each fluorescent single molecule punctum is described by a point spread function (PSF), which is fitted with a two-dimensional (2-D) Gaussian function using maximum-likelihood estimation to achieve sub-diffraction localization of single molecules.

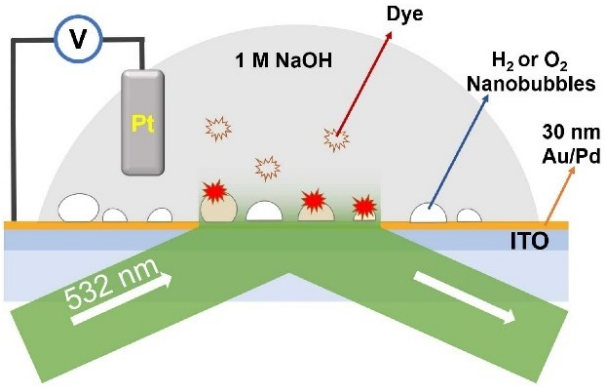

Figure 1. A schematic illustration of the electrochemical TIRF setup for imaging H_2 and O_2 nanobubbles on a metal-coated ITO electrode.

Results and Discussion

Figure 1 displays the electrochemical TIRF setup used for nanobubble imaging. An objective-based TIRF system was used to detect fluorescence signals of single molecules on a transparent electrode, which was an ITO electrode coated by a 30-nm Au/Pd film. A 532 nm laser was used to excite the fluorophores. The evanescent field selectively illuminates a thin solution layer (< 150 nm)[28] above the electrode surface, allowing one to image individual nanobubbles. Low concentrations (<20 nM) of Rhodamine 6G (R6G) solutions were used for nanobubble labeling. Due to their fast diffusion ($D = 4.0 \times 10^{-6}$ cm^2s^{-1})[29] and the fluorescence quenching near a conductor surface, freely diffusing R6G molecules can hardly be detected.[30,31] Only the fluorophores momentarily adsorbed and trapped at the nanobubble's gas/liquid interface can be observed.

We used a transparent Au/Pd-ITO electrode to nucleate both H_2 and O_2 nanobubbles at negative and positive potentials, respectively. These Au/Pd-ITO electrodes were fabricated by sputter coating a 30-nm film of gold/palladium (60:40, wt%) alloy on an ITO coverslip. The metal thickness was confirmed by profilometry. An Au/Pd-ITO electrode was mounted on an inverted TIRF microscope (Olympus IX70). The electrode surface was covered with a 200-μm-thick PDMS film and a round 2 mm region was exposed. A 10 μL solution containing 1 M NaOH was added onto the exposed electrode surface and a Pt wire was used as a QRE. The reaction on the Pt QRE is oxygen reduction or water oxidation at pH 14:

$$O_2(g) + 2H_2O + 4e^- \rightleftharpoons 4OH^- \ (E^\Theta = +0.40 \text{ V})^{32} \qquad (1)$$

which depends on the reaction on the working electrode (*i.e.*, OER or HER). Thus, for OER on the working electrode, a theoretical thermodynamic potential of 0 V (vs Pt QRE) can be expected. For HER at pH 14, the half reaction is as following,

$2H_2O + 2e^- = H_2(g) + 2OH^-$ ($E^{\ominus} = -0.83V$)[32] (2)

The theoretical thermodynamic reduction potential of the reaction should be -1.23V vs OER. Since the oxygen partial pressure in air is ~2.1×10^4 Pa, according to the Nernst equation, the potential of the HER should be -1.26 V vs Pt QRE.

Despite the successful detection of H_2 nanobubbles, we were unable to observe O_2 nanobubbles in our previous study. **Figure S1** shows a plot of the potential-dependent nanobubble detection frequency (# of detections per frame vs. potential) on a bare ITO electrode in 1 M NaOH. The absence of detections indicates no O_2 bubbles were detected on bare ITO in this potential range; this may be attributed to low catalytic activity of the ITO for the OER. To enhance the electrocatalytic activity of the electrode surface, we chose to deposit a thin film of Au/Pd for water electrolysis and detection of O_2 nanobubbles.

The small penetration depth of visible light in metal films[33] limits the maximum thickness of a metal film one can use for TIRF imaging. Burghardt and co-workers reported a metal film-enhanced total internal reflection microscopy with an Al film of only 30 nm.[34] A significant potential drop would occur inside the metal film due to the thin metal film's large ohmic resistance resulting in inaccurate control of the electrode potential. For optimized nanobubble detection, we used an ITO glass as a supporting substrate to enhance the conductivity of the thin Au/Pd film.

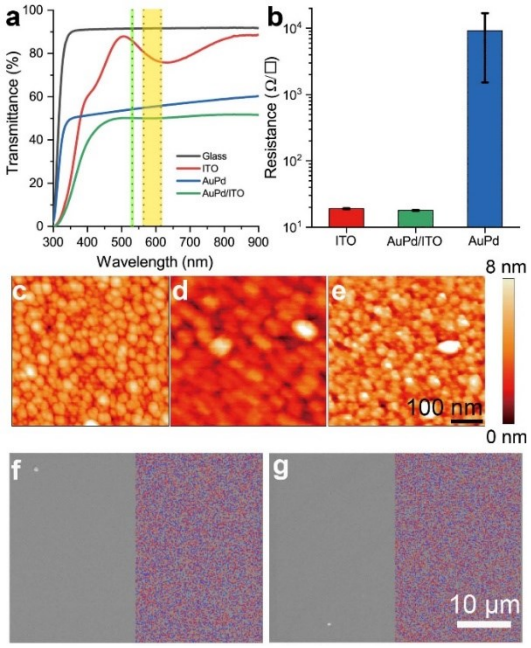

Figure 2. (a) UV-Vis transmittance spectra of four different substrates. The excitation wavelength (532 nm) and emission filter range (590±25 nm) were marked with dashed lines and tinted with corresponding color. (b) A bar chart showing the sheet resistance of the substrates. (c-e) AFM images of bare ITO surface (c), as prepared Au/Pd coated ITO surface (d) and Au/Pd coated ITO surface after 5 s activation at +0.5 V (e). (f, g) SEM images with left half of the image overlaying with corresponding EDS mapping results (red dots represent gold, blue dots represent palladium) of as prepared Au/Pd coated ITO surface (f) and Au/Pd coated ITO surface after 5 s activation at +0.5 V (g).

Prior to being used in electrochemical/fluorescence measurements, the Au/Pd-ITO electrodes were thoroughly characterized. **Figure 2a** displays UV-Vis transmittance spectra from 900 to 300 nm for four substrates: a 170-μm-thick glass coverslip, bare ITO coverslip (170-μm-thick), Au/Pd-coated glass coverslip, and Au/Pd-coated ITO. The glass coverslip (black line) exhibits high transmittance (~90%), while ITO (red line) shows 75% to 85% transmittance with a broad absorption peak around 650 nm. Both Au/Pd-coated substrates (blue and green lines) show even transmittance of visible light at 400 nm and higher; the transmittance values are ~50 % for Au/Pd on glass (blue line) and ~ 45% for Au/Pd on ITO (green line). A small but wide absorption peak can be found on Au/Pd on ITO, which should be related to the absorption peak of the ITO film. The excitation wavelength and emission filter used in this study were 532 nm and 590 ± 25 nm, respectively (shown in light green line and the yellow region). The transmittance values of the excitation/emission light are about

85%/75%, 50%/52% and 50%/50% for ITO, Au/Pd on glass and Au/Pd-coated ITO, respectively. Therefore, the detection probability of a fluorophore on a Au/Pd/glass electrode and a Au/Pd-ITO electrode would drop to ~40% of that on a bare ITO electrode. This is estimated by calculating the ratio of the product of the two transmittance values of a substrate vs that on the bare ITO. As such, the quality (signal/noise ratio) of the single-molecule signals will be somewhat compromised on a Au/Pd-ITO electrode.

The sheet resistances of the substrates are shown in **Figure 2b**. The electric resistance of the Au/Pd/glass substrate is around 10 KΩ/□ (Sheet Resistance, $R_s=\rho/t$, where ρ is the resistivity and t is the thickness of a material), which is several orders of magnitude higher than that of bare ITO and Au/Pd-ITO (~ 20 Ω/□). Therefore, the use of an ITO substrate greatly reduces the high ohmic resistance of thin metal film electrodes making them suitable for both electrochemical measurements and optical imaging. The sheet resistance of the films kept unchanged after a CV scan (0 V to -1.8 V to +0.5 V and back to 0 V, at 100 mV/s). We think this simple procedure could open up many new possibilities for exploring interfacial electrochemical processes with optical microscopy.

The surface morphology and chemical composition of the Au/Pd-ITO electrode were also studied. **Figure 2c-e** show AFM images of the bare ITO surface and surfaces of a Au/Pd-ITO electrode before and after electrochemical treatment. The bare ITO surface exhibits smooth and rounded domains with diameters of ~50 nm and heights of ~5 nm. The untreated Au/Pd-ITO electrode shows smoother features with larger domain sizes and lower surface roughness. After applying an oxidation potential of +0.5 V in 1 M NaOH, which serves as an activation step, the substrate begins to display a spiky morphology and the overall height of the features increases to around 8 nm. The surface morphologies are similar after the application of further oxidative treatments (**Figure S2 a**),

which indicates the morphology change could be self-limiting. Interestingly, the morphology appears to be smoother after a reductive treatment (**Figure S2 b**); this observation will be discussed in a later section.

Optical/electrochemical experiments confirmed that with activation (+0.5 V for 5 s) of the metal film, detection of nanobubbles is more reproducible. This type of activation strategy has been widely used elsewhere.[35] Scanning electron microscopy (SEM) and Energy-dispersive X-ray spectroscopy (EDS) were used to study the film morphology and surface composition across a larger area (hundreds of square microns). SEM images with EDS mapping of the electrode surface before (**Figure 2f**) and after the electrochemical treatment (**Figure 2g** and **Figure S2c, d**) indicate no obvious morphological or compositional changes occurred and the metal coating remains intact. EDS analyses of the mapped areas give the same Au/Pd ratio of 60/40 (wt%) for all samples. Although small nanoscopic changes can be found after the treatment, the Au/Pd on the ITO electrodes remained stable. Moreover, the formation of nanoscale features could serve as catalytic sites for the electrochemical reactions of interest.

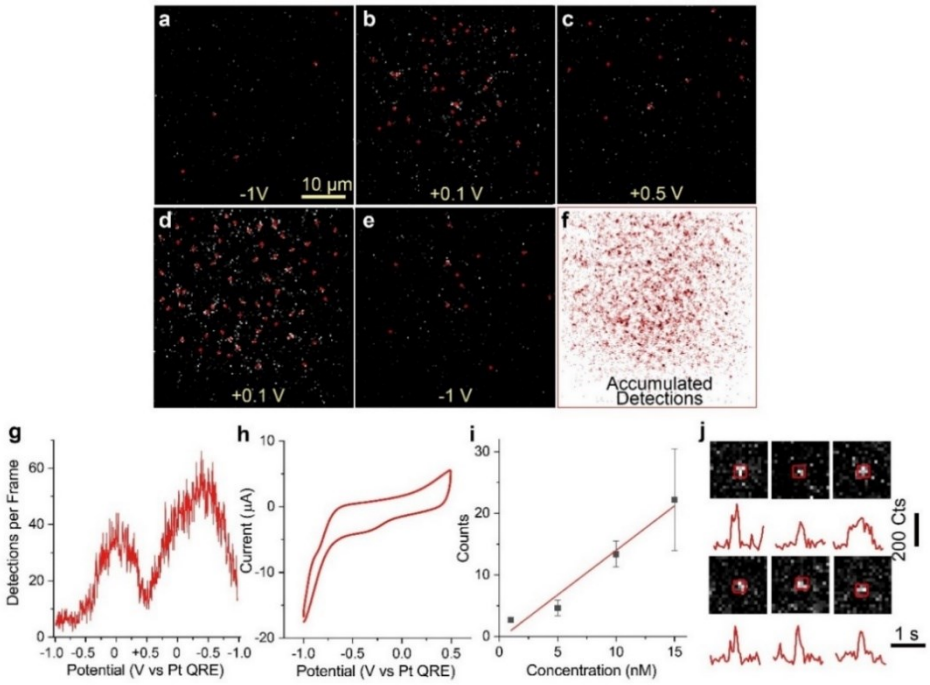

Figure 3. Imaging O_2 nanobubbles on the Au/Pd-ITO electrode. (a-e) A series of TIRF images showing detection of nanobubbles on electrode in a 1 M NaOH solution containing 15 nM R6G at different potentials in a triangular potential scan from -1 to +0.5 to -1 V vs Pt QRE at 100 mV/s. TIRF images were recorded at 19.81 frames/second with a 50-ms exposure time. Individual nanobubbles are located via super-resolution localization and marked with red crosses. (f) Accumulated detection results from the whole recording. (g) A potential dependent plot of nanobubble detection events (detection per frame) in the recording. (h) A typical CV response of an electrode in 1 M NaOH solution from -1 to +0.5 V (100 mV/s). (i) The average number of nanobubbles detected between +0.1 V and +0.2 V in the forward scan plotted vs R6G concentration. (j) Six fluorescence images and corresponding fluorescence intensity−time traces showing random selected nanobubbles detected at +0.1 V constant potential in 1 M NaOH solution containing 5 nM R6G. Each image was taken at the time point of peak intensity. The size of a pixel is 177.8 nm ×177.8 nm. Images were recorded at 19.81 frames per second with a 50-ms exposure time.

Oxygen nanobubbles were detected on the surface of the Au/Pd-ITO electrode by single-molecule fluorescence imaging. **Figure 3a-e** shows TIRF images of the electrode under different potentials (-1, 0.1, 0.5, 0.1, and -1 V) from a CV scan (-1 to +0.5 to -1 V, 100 mV/s) in 1 M NaOH containing 15 nM R6G. Super-resolution localization was used to locate the fluorescent puncta (red crosses). The discrete fluorescent puncta can be observed in the images collected in the potential range of 0 to +0.5 V, indicating successful labeling of oxygen nanobubbles with R6G molecules. We believe nanobubbles are labeled with single molecules, which is similar to our previous result.[21] This will be further discussed in a later section on the concentration dependence experiments of the dye molecules.

The number of fluorescent punctum detections (nanobubble events) in each frame was plotted versus the applied potential (**Figure 3g**). An increase in the number of detections can be observed at around -0.4 V, which reaches a peak at ~0 V followed by a decay as the potential was further increased. The increase from -0.4 to 0 V is likely due to faster OER kinetics at higher driving potentials. The decay from 0 V to +0.5 V, however, should be due to an increase in nanobubble size, which “lifts” the R6G molecules from being effectively excited by the evanescent wave. A similar

trend of an initial increase followed by a decay in the number of nanobubbles was previously observed in our previous study for H_2 nanobubbles.[21] Our hypothesis of R6G being more effectively "lifted" by larger nanobubbles at higher driving potentials was supported by a uniform decaying fluorescence intensity, which, in TIRF-based imaging, often translates to greater fluorophore-substrate distance.

The number of detections increased as the potential was scanned back from +0.5 V, consistent with our expectation. Interestingly, the number of detections per frame kept increasing passing 0 V to a new peak at ~-0.4 V, which then decayed back as the potential was further decreased. In addition to the somewhat delayed peak position, the highest number of detections also increased from ~35 bubbles/frame to 55 bubbles/frame. The exact reasons to the delayed peak position and the higher peak value are unclear at this moment. However, we believe they are related to the change in the local O_2 concentration as well as the high stability of surface-supported nanobubbles.

It is also interesting to observe that the number of detections did not drop to its initial value, ~6 bubbles/frame, as the potential was swept from -0.5 back to -1.0 V. In fact, there were still ~20 nanobubbles detected in each frame. This result suggests that some nanobubbles were still present on the electrode after the potential scan was finished and there was no longer enough potential driving force to support them. This observation is again in agreement with the higher peak value on the reverse scan and can be understood by nanobubble's high stability.

Figure 3h shows a CV recording of a typical Au/Pd-ITO electrode under the same conditions. The onset potential of OER is around +0.1 V. The different onset potentials in fluorescence recording and electrochemical recording suggest that oxygen nanobubbles could be generated at a very early stage of the OER, which is consistent with our previous observation describing hydrogen nanobubble

generation on an ITO electrode.[21] Highly active catalytic sites could serve as nucleation centers for the gas evolution reaction. **Figure 3f** shows accumulated single fluorescent puncta locations throughout the entire CV scan. The image shows a roughly even distribution with certain locations exhibiting higher puncta density, thereby indicating possible sites of increased activity. An *in situ* correlated surface morphology (SPM) and optical microscopy study on this issue is under way. In the accumulated detection plot, there are fewer detections at the edge of the image than at the center. This observation is due to slight non-uniformity of the laser beam.

When the fluorophore concentration is sufficiently low, e.g., a few nM, most nanobubbles are labeled by a single fluorophore molecule. Thus, within a certain concentration range and at a constant potential, an increase in the fluorophore concentration should allow more nanobubbles to be labeled and the number of nanobubble detections per frame should roughly be proportional to the fluorophore concentration. For imaging oxygen nanobubbles, we kept R6G concentrations of 1, 5, 10, and 15 nM. To compare the number of nanobubble detections at different dye concentrations, we used the optimum range of potentials, +0.1 to +0.2 V (vs Pt QRE) for oxygen bubble detection. Sporadic puncta can be observed with 1 nM R6G while the entire field of view is full of detections when R6G concentration was increased to 15 nM. Over-lapping of puncta leads to increased difficulty of achieving single molecule resolution at higher R6G concentrations. After plotting the average number of detections per frame within the aforementioned potential window against the R6G concentration in **Figure 3i**, a nearly linear correlation was found between the number of detected nanobubble and the fluorophore concentration in agreement with our prediction.

To further verify our hypothesis of single molecule labeling, oxygen nanobubbles were generated under a constant potential (+0.1 V) and individual nanobubbles were imaged for analysis. **Figure 3j**

shows six randomly selected nanobubble detection events from a 50 s recording. Each nanobubble detection event is shown with a fluorescent punctum image (upper part) and corresponding intensity–time trace (lower part). These events last from 50 ms to 200 ms with the average intensities of each pixel within the squared areas ranging from 100 to 200 counts. These representative detection results suggest single molecular on-off type behavior. It is worth mentioning that the detections are very transient and elusive, a phenomenon that is likely due to the strong fluorescence-quenching ability of metal which is several times stronger than ITO[36] and/or the fast adsorption/desorption kinetics of R6G molecules on the nanobubble surface.[37]

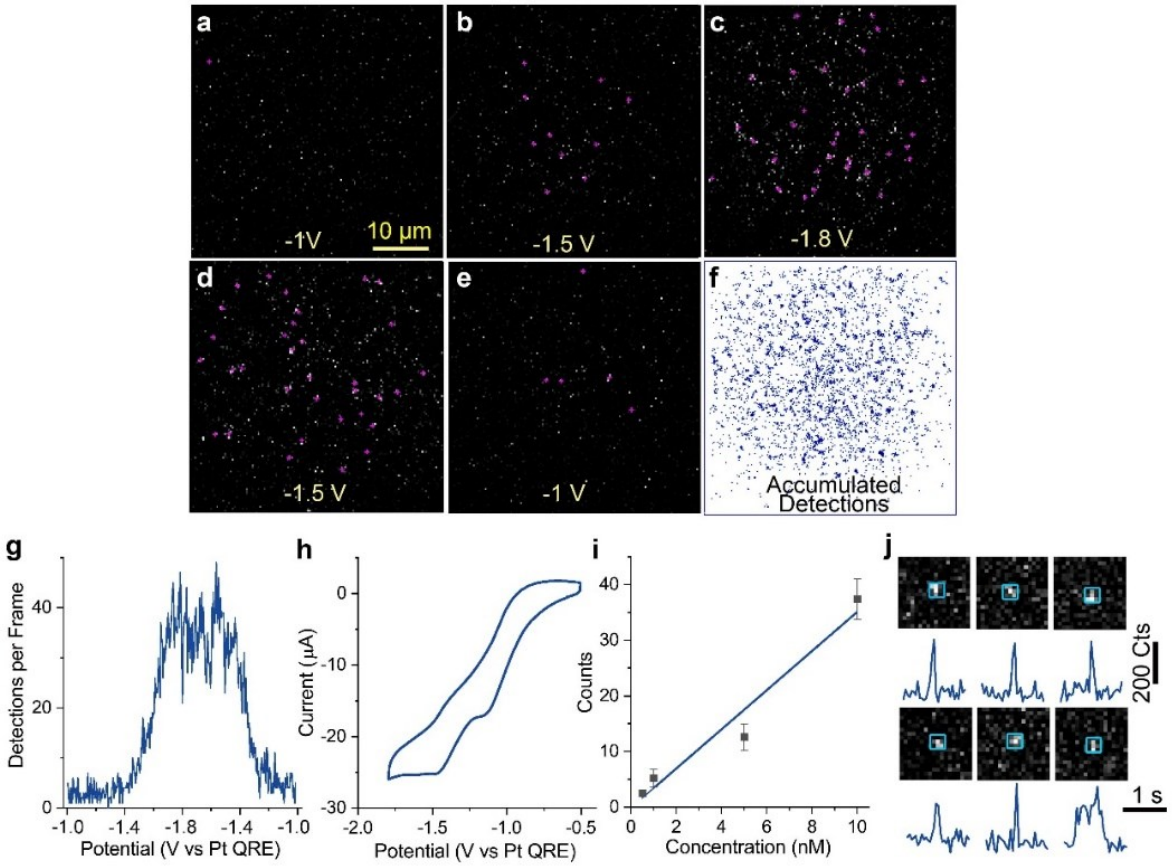

Figure 4. Imaging H_2 nanobubbles on the Au/Pd-ITO electrode. (a-e) (A series of TIRF images showing nanobubbles on electrode in 1 M NaOH solution containing 10 nM R6G at different potentials from a triangular potential scan from -1 to -1.8 to -1 V at 100mV/s. TIRF images were recorded at 19.81 frames/second with a 50-ms exposure time. The nanobubble detection events are located via super-resolution localization technique and marked with violet crosses. (f) Accumulated detection results from the whole recording. (g) A potential dependent plot of nanobubble detection events (detection per frame) in the same recording. (h) A typical CV

response of an electrode in 1 M NaOH solution from -0.5 to -1.8 V (100 mV/s). (i) The average number of nanobubbles detections between -1.5 and -1.8 V in the forward scan plotted vs R6G concentration. (j) Six fluorescence images and corresponding fluorescence intensity−time traces showing random selected nanobubbles detected at -1.5 V constant potential in 1 M NaOH solution containing 5 nM R6G. Each image was taken at the time point of peak intensity. The size of a pixel is 177.8 nm ×177.8 nm. Images were recorded at 19.81 frames/second with a 50-ms exposure time.

We further examined the detection of hydrogen nanobubbles on a Au/Pd-ITO electrode by scanning the electrode potential in a range of -1 to -1.8 V. **Figure 4a-e** shows a series of fluorescence images of H_2 nanobubble detection events at -1, -1.5, -1.8, -1.5 and -1 V from a voltage scan on the electrode in 1 M NaOH containing 10 nM R6G. Fluorescent puncta (which represents nanobubble generation) are highlighted with purple crosses in the images. **Figure 4b-d** shows a large number of detections, whereas only a few detections are visible at -1 V (**Figure 4a**, **e**). The detection count per frame was plotted versus applied potential in **Figure 4g**. A rapid increase in the detection number is observed at around -1.4 V in the forward scan. This value peaks at around -1.8 V then deceases. At around -1.5 V another peak may be observed which rapidly decays to baseline at around -1.3 V. The shape of the curve is somewhat symmetric, but the center is at -1.6 V in the reverse scan, thereby demonstrating a hysteretic response to the applied potential. The accumulated event location image in **Figure 4f** shows a similar feature as in the oxygen evolution case, suggesting some degree of heterogeneity in the electrode surface.

A typical CV response of a Au/Pd-ITO electrode was also recorded (**Figure 4h**). The first reduction wave with an onset potential of -0.75 V is attributed to ORR. The large over potential of 0.75 V suggests that the substrate materials in their current form are not an ideal electrocatalyst for ORR (which is also outside the scope of this study). In our previous report on water reduction, the ORR peak was not observed on bare ITO electrode likely due to ITO's poor electrocatalytic activity.

The second wave at around -1.3 V should be assigned to water reduction/hydrogen evolution

reaction. This value is in very good agreement with the theoretical onset potential of -1.26 V vs Pt QRE discussed above. As shown in **Figure 4g** (potential vs number of detection plot), there is an obvious generation of H_2 nanobubbles beginning at a more negative potential than -1.4 V. Very early stage generation of H_2 nanobubbles on ITO was observed in our previous study and a similar phenomenon was also confirmed in the oxygen evolution case in this study. The somewhat "delayed" generation of H_2 nanobubbles which we observed is likely due to the electrode materials we employed. Palladium exhibits unmatched hydrogen storage ability in its pure form. It has also been reported that gold-palladium alloy exhibits hydrogen absorption/storage ability.[38] Therefore, the electrochemically-generated hydrogen atoms may have a high tendency to dissolve in the metal electrode before forming H_2 molecules and nucleating into nanobubbles. The hysteretic response of nanobubble generation we observed therefore seems reasonable. We mentioned in the previous section (**Figure S2 b**) that the fine surface morphology was altered after the application of reductive potentials. This transformation could also be due to lattice expansion of the alloy caused by hydrogen insertion.[39] Moreover, hydrogen oxidation on gold/palladium is very efficient; any H_2 bubbles generated on the electrode surface can be easily consumed as soon as a sufficiently positive potential is applied. A drastic decrease in the number of detected nanobubbles at around -1.3 V can therefore be observed. Thus, the curve of nanobubble detection in the hydrogen evolution case is somewhat symmetrical.

A concentration dependence experiment was also carried out for H_2 nanobubble detection at four different R6G concentrations (0.5, 1, 5, and 10 nM). The average number of detections per frame in the range of -1.5 to -1.8 V in the forward CV scan was plotted against concentration in **Figure 4i**. The nearly linear correlation, which is like the O_2 nanobubble case, is indicative of the single molecular

labeling process. Single-molecule type behavior can also be confirmed by the randomly-selected fluorescence detections collected at a constant potential of -1.5 V shown in **Figure 4j**. These fluorescence events show intensity values of around 150 counts and durations of around 100 ms, thereby demonstrating on-off behaviors which confirm our single-molecule labeling process.

Conclusions

In summary, we have used metal-coated ITO as an effective electrode material for single-molecule fluorescence imaging of nanobubbles. Nanobubbles of both O_2 and H_2 have been generated on a gold/palladium-modified ITO electrode from the overall water electrolysis demonstrating the use of this electrode for nanobubble study. Our results show that O_2 nanobubbles can be generated at an early stage in the OER on the Au/Pd-ITO electrode. H_2 nanobubbles, one the other hand, exhibit delayed generation, which is likely due to the hydrogen storage property of the Au/Pd alloy. The use of a thin metal film to modify an ITO electrode is a simple and reproducible method to prepare highly conductive and transparent electrodes for single-molecule spectroelectrochemistry research.

Acknowledgement

This research was supported by the National Science Foundation (CHE-1904426). Part of this work was conducted at the Molecular Analysis Facility, a National Nanotechnology Coordinated Infrastructure site at the University of Washington which is supported in part by the National Science Foundation (grant ECC-1542101), the University of Washington, the Molecular Engineering & Sciences Institute, the Clean Energy Institute, and the National Institutes of Health.

Associated Content

Supporting Information. Experimental Section, Nanobubble detection on bare ITO, additional AFM/SEM images of the modified ITO electrode, and fluorescence emission spectra of 1 μM R6G in 1 M NaOH. This information is available free of charge on the ACS Publications website.

Notes

The authors declare no competing financial interest.

References:

1. You, B.; Sun, Y. Innovative Strategies for Electrocatalytic Water Splitting. *Acc. Chem. Res.* **2018**, *51*, 1571–1580.
2. Rossmeisl, J.; Logadottir, A.; Norskov, J. K. Electrolysis of Water on (Oxidized) Metal Surfaces. *Chem. Phys.* **2005**, *319*, 178–184.
3. Kim, J. S.; Kim, B.; Kim, H.; Kang, K. Recent Progress on Multimetal Oxide Catalysts for the Oxygen Evolution Reaction. *Adv. Energy Mater.* **2018**, *8*, 1702774.
4. Li, X.; Hao, X.; Abudula, A.; Guan, G. Nanostructured Catalysts for Electrochemical Water Splitting: Current State and Prospects. *J. Mater. Chem. A* **2016**, *4*, 11973–12000.
5. Zhao, X.; Ren, H.; Luo, L. Gas Bubbles in Electrochemical Gas Evolution Reactions. *Langmuir* **2019**, *35*, 5392–5408.
6. Li, J.; Zhu, Y.; Chen, W.; Lu, Z.; Xu, J.; Pei, A.; Peng, Y.; Zheng, X.; Zhang, Z.; Chu, S.; et al. Breathing-Mimicking Electrocatalysis for Oxygen Evolution and Reduction. *JOULE* **2019**, *3*, 557–569.
7. Lu, Z.; Zhu, W.; Yu, X.; Zhang, H.; Li, Y.; Sun, X.; Wang, X.; Wang, H.; Wang, J.; Luo, J.; Lei, X.; Jiang, L. Ultrahigh Hydrogen Evolution Performance of Under-Water "Superaerophobic" MoS2 Nanostructured Electrodes. *Adv. Mater.* **2014**, *26*, 2683–2687.
8. Lohse, D.; Zhang, X. Surface Nanobubbles and Nanodroplets. *Rev. Mod. Phys.* **2015**, *87*, 981–1035.
9. Ishida, N.; Inoue, T.; Miyahara, M.; Higashitani, K. Nano Bubbles on a Hydrophobic Surface in Water Observed by Tapping-Mode Atomic Force Microscopy. *Langmuir* **2000**, *16*, 6377–6380.
10. Karpitschka, S.; Dietrich, E.; Seddon, J. R. T.; Zandvliet, H. J. W.; Lohse, D.; Riegler, H. Nonintrusive Optical Visualization of Surface Nanobubbles. *Phys. Rev. Lett.* **2012**, *109*, 1–5.
11. Chan, C. U.; Ohl, C.-D. D. Total-Internal-Reflection-Fluorescence Microscopy for the Study of Nanobubble Dynamics. *Phys. Rev. Lett.* **2012**, *109*, 174501.
12. Su, H.; Fang, Y.; Chen, F.; Wang, W. Monitoring the Dynamic Photocatalytic Activity of Single CdS Nanoparticles by Lighting Up H2 Nanobubbles with Fluorescent Dyes. *Chem. Sci.* **2018**, *9*, 1448.
13. Li, S.; Du, Y.; He, T.; Shen, Y.; Bai, C.; Ning, F.; Hu, X.; Wang, W.; Xi, S.; Zhou, X. Nanobubbles: An Effective Way to Study Gas-Generating Catalysis on a Single Nanoparticle. *J. Am. Chem. Soc.* **2017**, *139*, 14277–14284.
14. Chen, J.; Zhou, K.; Wang, Y.; Gao, J.; Yuan, T.; Pang, J.; Tang, S.; Chen, H.-Y. Y.; Wang, W. Measuring the Activation Energy Barrier for the Nucleation of Single Nanosized Vapor Bubbles. *Proc. Natl. Acad. Sci.* **2019**, *116*, 12678–12683.
15. Chen, Q.; Luo, L.; Faraji, H.; Feldberg, S. W.; White, H. S. Electrochemical Measurements of Single H2

Nanobubble Nucleation and Stability at Pt Nanoelectrodes. *J. Phys. Chem. Lett.* **2014**, *5*, 3539–3544.
16. Smeets, R. M. M.; Keyser, U. F.; Wu, M. Y.; Dekker, N. H.; Dekker, C. Nanobubbles in Solid-State Nanopores. *Phys. Rev. Lett.* **2006**, *97*, 1–4.
17. Hu, Y.-X. X.; Ying, Y.-L. L.; Gao, R.; Yu, R.-J. J.; Long, Y.-T. T. Characterization of the Dynamic Growth of the Nanobubble within the Confined Glass Nanopore. *Anal. Chem.* **2018**, *90*, 12352–12355.
18. Han, C.; Hao, R.; Fan, Y.; Edwards, M. A.; Gao, H.; Zhang, B. Observing Transient Bipolar Electrochemical Coupling on Single Nanoparticles Translocating through a Nanopore. *Langmuir* **2019**, *35*, 7180–7190.
19. Sundaresan, V.; Monaghan, J. W.; Willets, K. A. Visualizing the Effect of Partial Oxide Formation on Single Silver Nanoparticle Electrodissolution. *J. Phys. Chem. C* **2018**, *122*, 3138–3145.
20. Hao, R.; Fan, Y.; Zhang, B. Imaging Dynamic Collision and Oxidation of Single Silver Nanoparticles at the Electrode/Solution Interface. *J. Am. Chem. Soc.* **2017**, *139*, 12274–12282.
21. Hao, R.; Fan, Y.; Howard, M. D.; Vaughan, J. C.; Zhang, B. Imaging Nanobubble Nucleation and Hydrogen Spillover during Electrocatalytic Water Splitting. *Proc. Natl. Acad. Sci.* **2018**, *115*, 5878–5883.
22. Sambur, J. B.; Chen, P. Approaches to Single-Nanoparticle Catalysis. *Annu. Rev. Phys. Chem.* **2014**, *65*, 395–422.
23. Matveeva, E. Electrochemistry of the Indium-Tin Oxide Electrode in 1 M NaOH Electrolyte. *J. Electrochem. Soc.* **2005**, *152*, H138.
24. Amiri, M.; Fallahi, M.; Bezaatpour, A.; Jijie, R.; Nozari-asbmarz, M.; Rouhi, M.; Boukherroub, R.; Szunerits, S. Solution Processable Cu(II) Macrocycle for the Formation of Cu2O Thin Film on Indium Tin Oxide and Its Application for Water Oxidation. *J. Phys. Chem. C* **2018**, *122*, 16510–16518.
25. Oja, S. M.; Wood, M.; Zhang, B. Nanoscale Electrochemistry. *Anal. Chem.* **2013**, *85*, 473–486.
26. Oja, S. M.; Fan, Y.; Armstrong, C. M.; Defnet, P.; Zhang, B. Nanoscale Electrochemistry Revisited. *Anal. Chem.* **2016**, *88*, 414–430.
27. Ovesný, M.; Křížek, P.; Borkovec, J.; Švindrych, Z.; Hagen, G. M. ThunderSTORM: a comprehensive ImageJ plug-in for PALM and STORM data analysis and super-resolution imaging. *Bioinformatics* **2014**, *30*, 2389–2390.
28. Martin-Fernandez, M. L.; Tynan, C. J.; Webb, S. E. D. A “pocket Guide” to Total Internal Reflection Fluorescence. *J. Microsc.* **2013**, *252*, 16–22.
29. Gendron, P.-O.; Avaltroni, F.; Wilkinson, K. J. Diffusion Coefficients of Several Rhodamine Derivatives as Determined by Pulsed Field Gradient–Nuclear Magnetic Resonance and Fluorescence Correlation Spectroscopy. *J. Fluoresc.* **2008**, *18*, 1093.
30. Fan, Y.; Hao, R.; Han, C.; Zhang, B. Counting Single Redox Molecules in a Nanoscale Electrochemical Cell. *Anal. Chem.* **2018**, *90*, 13837–13841.
31. Lu, J.; Fan, Y.; Howard, M. D.; Vaughan, J. C.; Zhang, B. Single-Molecule Electrochemistry on a Porous Silica-Coated Electrode. *J. Am. Chem. Soc.* **2017**, *139*, 2964–2971.
32. Bratsch, S. G. Standard Electrode Potentials and Temperature Coefficients in Water at 298.15 K. *J. Phys. Chem. Ref. Data* **1989**, *18*, 1–21.
33. Axelevitch, A.; Gorenstein, B.; Golan, G. Investigation of Optical Transmission in Thin Metal Films. *Phys. Procedia* **2012**, *32*, 1–13.
34. Burghardt, T. P.; Charlesworth, J. E.; Halstead, M. F.; Tarara, J. E.; Ajtai, K. In Situ Fluorescent Protein Imaging with Metal Film-Enhanced Total Internal Reflection Microscopy. *Biophys. J.* **2006**, *90*, 4662–4671.

35. Han, C.; Percival, S. J.; Zhang, B. Electrochemical Characterization of Ultrathin Cross-Linked Metal Nanoparticle Films. *Langmuir* **2016**, *32*, 8783–8792.
36. Moerland, R. J.; Hoogenboom, J. P. Subnanometer-Accuracy Optical Distance Ruler Based on Fluorescence Quenching by Transparent Conductors. *Optica* **2016**, *3*, 112–117.
37. Zheng, X.-Y.; Harata, A.; Ogawa, T. Study of the Adsorptive Behavior of Water-Soluble Dye Molecules (Rhodamine 6G) at the Air–Water Interface Using Confocal Fluorescence Microscope. *Spectrochim. Acta Part A Mol. Biomol. Spectrosc.* **2001**, *57*, 315–322.
38. Łukaszewski, M.; Kuśmierczyk, K.; Kotowski, J.; Siwek, H.; Czerwiński, A. Electrosorption of Hydrogen into Palladium-Gold Alloys. *J. Solid State Electrochem.* **2003**, *7*, 69–76.
39. Łukaszewski, M.; Czerwiński, A. Electrochemical Behavior of Palladium–Gold Alloys. *Electrochim. Acta* **2003**, *48*, 2435–2445.

For Table of Contents Only